
Original Articles

Automated Detection of Tunneling Nanotubes in 3D Images

Erlend Hodneland,¹ Arvid Lundervold,^{1*} Steffen Gurke,² Xue-Cheng Tai,³
Amin Rustom,² and Hans-Hermann Gerdes^{1,2}

¹Department of Biomedicine, University of Bergen, Bergen, Norway

²Interdisciplinary Center of Neuroscience (IZN), Institute of Neurobiology, University of Heidelberg, Heidelberg, Germany

³Department of Mathematics, University of Bergen, Bergen, Norway

Received 13 October 2005; Revision Received 24 February 2006; Accepted 12 April 2006

Background: This paper presents an automated method for the identification of thin membrane tubes in 3D fluorescence images. These tubes, referred to as tunneling nanotubes (TNTs), are newly discovered intercellular structures that connect living cells through a membrane continuity. TNTs are 50–200 nm in diameter, crossing from one cell to another at their nearest distance. In microscopic images, they are seen as straight lines. It now emerges that the TNTs represent the underlying structure of a new type of cell-to-cell communication.

Methods: Our approach for the identification of TNTs is based on a combination of biological cell markers and known image processing techniques. Watershed segmentation and edge detectors are used to find cell borders, TNTs, and image artifacts. Mathematical morphology is employed at several stages of the processing chain. Two image channels are used for the calculations to improve classification of watershed regions into cells and background. One image channel displays cell borders and TNTs, the second is used for cell classification and dis-

plays the cytoplasmic compartments of the cells. The method for cell segmentation is 3D, and the TNT detection incorporates 3D information using various 2D projections.

Results: The TNT- and cell-detection were applied to numerous 3D stacks of images. A success rate of 67% was obtained compared with manual identification of the TNTs. The digitalized results were used to achieve statistical information of selected properties of TNTs.

Conclusion: To further explore these structures, automated detection and quantification is desirable. Consequently, this automated recognition tool will be useful in biological studies on cell-to-cell communication where TNT quantification is essential. © 2006 International Society for Analytical Cytology

Key terms: tunneling nanotubes; cell imaging; segmentation; mathematical morphology; classification; image processing; computer vision and recognition

Recently, Rustom et al. (1) described thin, membranous tubes that represent an independent form of cell-to-cell communication, termed tunneling nanotubes (TNTs). TNTs form in cultures of a variety of cells, have a diameter of 50–200 nm, and connect cells, resulting in complex networks. These fragile, actin-rich structures were shown to transport organelles of endocytic origin from one cell to another in an unidirectional fashion, and to a limited amount also membrane components (1). In addition, they were shown to transfer actin, a structural component of the TNT itself. On the basis of these data, Rustom and coworkers have proposed a novel biological principle of cell-to-cell interaction based on membrane continuity and intercellular transfer of organelles. Subsequent studies have shown comparable membrane channels in variegated cellular systems (2). In the case of immune cells, the

TNT connectors (3) have been shown to transfer a calcium signal into the connected cell (4). Thus, it emerges that TNTs fulfill important functions in intercellular communication. Provided that TNTs are present in tissue, they may have numerous implications in cellular signaling, including the spread of morphogens during developmen-

Grant sponsor: Norwegian Cancer Society; Grant sponsor: Stiftelsen Universitetsforskning Bergen (UNIFOB AS); Grant sponsor: Deutsche Forschungsgemeinschaft; Grant numbers: SFB 488/B2, GE 550/3-2.

*Correspondence to: Arvid Lundervold, Neuroinformatics and Image Analysis Group, Department of Biomedicine, University of Bergen, Jonas Lies vei 91, N-5009 Bergen, Norway.

E-mail: arvid.lundervold@biomed.uib.no

Published online in Wiley InterScience (www.interscience.wiley.com).

DOI: 10.1002/cyto.a.20302

tal processes, intercellular spread of immunogenic material (3), and spread of pathogens. TNTs resemble membrane connections between plant cells, known as plasmodesmata. Plasmodesmata are of great importance for the intercellular exchange of signaling molecules, and it has been reported that viruses are able to migrate through these membrane tubes from one cell to another (5). The strong resemblance between plasmodesmata and TNTs suggests that the latter may fulfill similar important functions in animal cells. Consequently, it is of great interest for cell biology to increase the knowledge about these structures.

The occurrence of TNTs inside a 3D image stack can usually be spotted by a trained eye, and in many cases humans can perform a better job than the computer. However, using human resources when collecting quantitative information about TNTs in large collections of data is extremely demanding and expensive. Moreover, the counting of TNTs based on visual inspection is subject to interobserver and intraobserver variability. TNTs frequently cross several planes, requiring 3D analysis in searching for TNTs, a challenging task for humans. Cell biologists are interested in manipulating the formation of TNTs to monitor their role in pathogenesis of various diseases, such as in cell-to-cell communication during growth of cancer or in immunological processes. This manipulation of TNTs requires quantitative analysis of their formation to gain statistical information. Automated or semiautomated procedures for finding and characterizing TNTs in image recordings will thus be an important tool for facilitating TNT research.

Our approach for finding TNTs is based on binary classification of the image into cells and background. Detection and classification of cells in microscopic images is a large area of research, with a long history within biomedical imaging (6–8). Commercially available software packages for cell counting and cell characterization are available for clinical and research use (9). However, it is important to keep in mind that these packages are very specialized, depending on specimen preparation, sectioning and staining, as well as imaging method, spatial resolution, and the kind of cells and artifacts being imaged. In the following, some studies related to cell detection are presented. These studies have applied methods that inspired our design principles in the way they have been dealing with similar recognition tasks. Wählby et al. (10) obtained between 89% and 97% correct classification of cells using a watershed segmentation method with double thresholds for detecting CHO cells in fluorescence microscopy images. Watershed segmentation is especially well suited for images containing natural minima surrounded by ridges. By calculating a Mahalanobis distance between feature vectors associated to the objects, a quality measure for the classification of cells, background, and artifacts was obtained. For splitting of undersegmented objects they used the convex hull for locating concavities, assuming that cells have concave like shapes, which may not always be true. Ellipsoidal shaped cells can also be found from a matching template. In this respect, Yang and Jiang (11) proposed a segmentation method using kernel-based

dynamic clustering and a matching ellipsoidal cell model. However, cells are not always ellipsoidal shaped, but frequently display a nonconvex appearance. For this, Garrido and de la Blanca (12) used deformable templates to identify cells under conditions with substantial noise. They applied a generalized Hough transform with a relatively large region of uncertainty which was used to roughly detect round-like shapes. These elliptic structures were later used as input for the Grenander deformable template model to fit the cell borders more accurately. For nuclei stained cells, Mouroutis et al. (13) proposed a method for finding possible locations of cell nuclei using a Compact Hough Transform (CHT). Their CHT assumes that the cells are convexly shaped, so that all boundary points of a cell lie within a maximal and a minimal distance from the nuclear centroid. A maximization of probability was used in combination with the CHT to find the possible nuclear boundaries.

TNT detection itself requires other approaches than those used for cell detection. Automated TNT detection has not been previously reported, and relevant detection problems with similar characteristics will therefore be discussed below. These problems deal with detection of straight line segments, partly using edge-detectors and Hough transformations. Nath and Depona (14) applied Canny's edge detector to find edges of a DNA protein, followed by an active contour model, a snake, for identification of the exact and connected curve surrounding the protein. However, the snake model could only detect one DNA protein, even in the presence of many, and leaving it to the user to seed the snake initially. Niesmistö et al. (15) used image analysis methods to quantify angiogenesis which was influenced by stimulatory and inhibitory agents. Their method gave length and number of junctions of the tubule complexes, applying thresholding and thinning to detect the thin blood vessels. From quite another field, automated detection of bridges in high-resolution satellite images is a strikingly similar problem to our task of TNT detection. Lomenie et al. (16) reported a low rate of false positive (~5%) but also a low success rate (~40%) for their algorithm. They explored both textural and geometric approaches. The textural approach was used to classify each pixel into type of terrain using a neural network, and thereafter they applied selection rules to the image. Their geometric approach was based on edge filtering and search for parallel neighbor-segments as candidates for bridges. For the same problem, Jeong and Takagi (17) used a Prewitt filter and Hough transformation to detect the bridge constructions that appear as straight lines.

Several ideas from the previous work described above, like watershed segmentation, Hough transformation, and edge detectors, have been applied for the task of TNT detection and quantification. However, finding so extreme thin structures as TNTs automatically is such a great challenge that in addition to the cell borders, the cell interior had to be labeled by a fluorescence marker. This cell marker created a second image channel, mark-

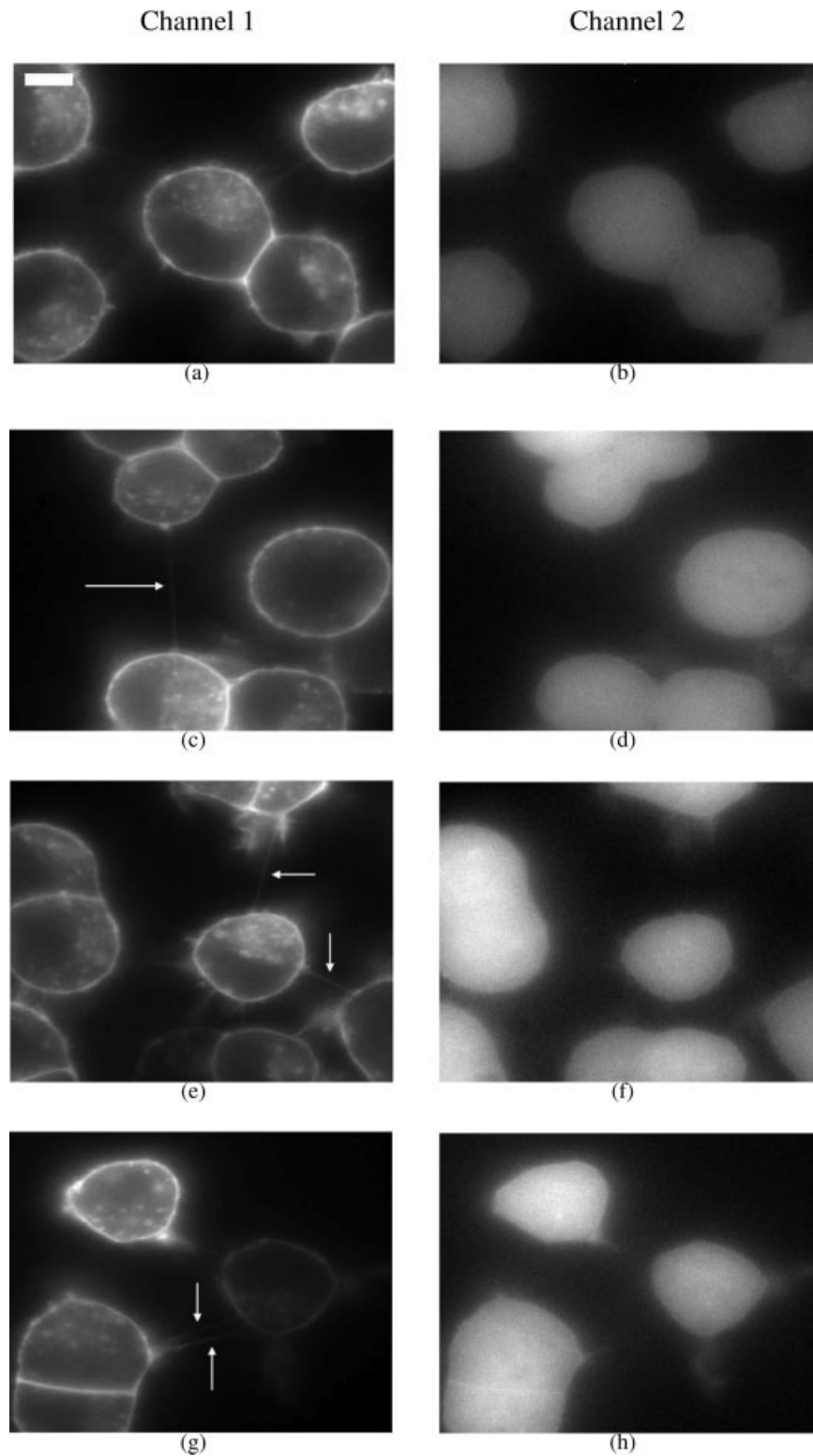


FIG. 1. A selection of representative images used for TNT detection. The left column shows TNTs and cell borders, the right column shows the cytoplasmic areas of the cells. Corresponding left and right images are taken from the same optical plane of the biological sample. Clearly visible TNTs are marked with arrows, and the white bar in (a) corresponds to 5 μm .

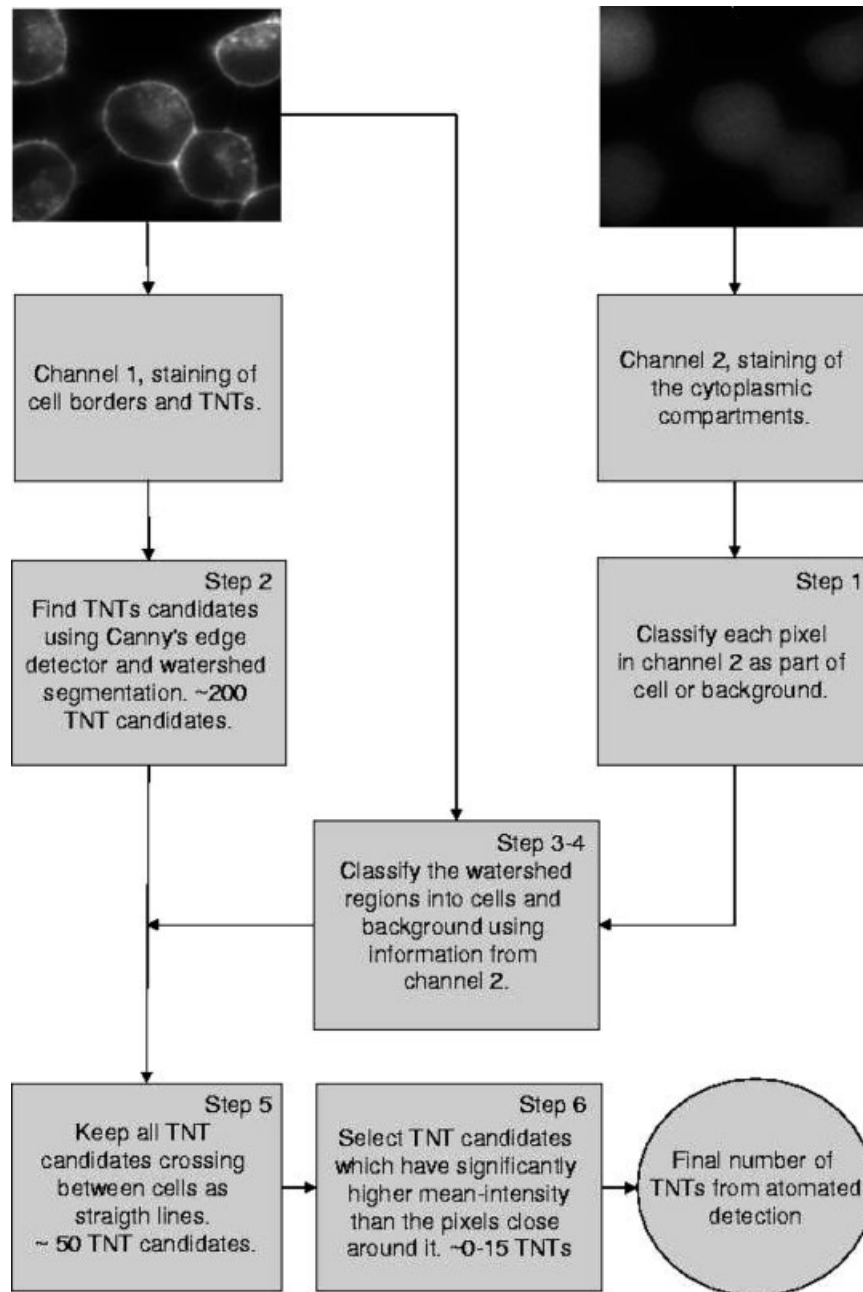


FIG. 2. Flow-scheme of the algorithm for automated detection of TNTs. The stepwise numbering refers to the numbers in section Description of Each Processing Step.

ing the cells as light regions and background as dark regions. The cell marker itself provides not sufficient information to distinguish each cell from other cells, but it can distinguish cells from background. The processing steps presented in this paper are developed so as to enable identification of which pair of cells each TNT is connecting. The chain of processing steps we have designed, incorporates generic methods from digital filtering [including deblurring with Richardson-Lucy (RL) deconvolution], edge detection (Canny's edge detector), and mathematical morphology (including watershed seg-

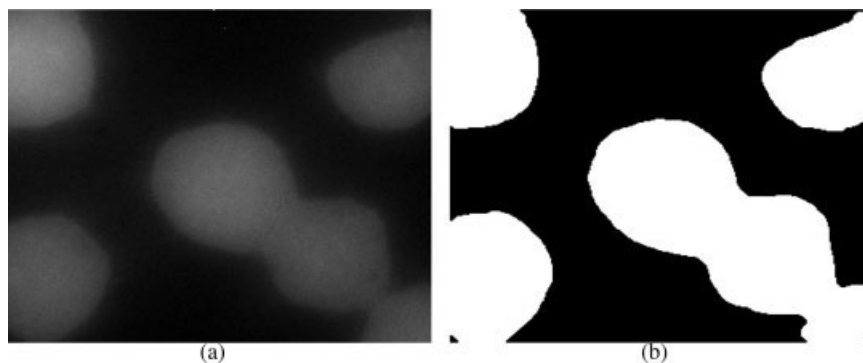
mentation). All algorithms at different steps are implemented for 3D images, either using entirely 3D based operations, or assisted by specialized projections, assimilating 3D information into 2D images.

MATERIALS AND METHODS

Preparation of the Microscopic Images

All image analyses were carried out with PC12 cells [rat pheochromocytoma cells, clone 251, (18)]. This neuroendocrine cell line was first generated in 1976 by Greene

FIG. 3. Segmentation of cellular regions into a binary mask. The cell marker image (a) has been segmented (b) into extracellular (black) and intracellular (white) regions.



and Tischler (19) as a single cell clonal line that grows in mono-layers forming small clusters. PC12 cells respond reversibly to nerve growth factor and have been used as a neuronal cell model. Recently, it has been shown that these cells form TNTs (1), which are subject to the present study. PC12 cells were cultured in DMEM supplement with 10% fetal calf serum and 5% horse serum at 37°C and 10% CO₂ in 15 cm dishes. For light microscopic analysis, PC12 cells were plated in LabTek™ chambered four-well coverglasses (Nalge Nunc Int., Wiesbaden, Germany).

PC12 cells were stained with two dyes, one displaying the cell borders and TNTs [wheat germ agglutinin (WGA) Alexa Fluor® 594, Molecular Probes], the other displaying cytoplasm (CellTracker™, Molecular Probes, Eugene, OR). WGA Alexa Fluor® is a lectin that binds glycoconjugates like N-acetylglucosamine and therefore stains biological membranes efficiently. CellTracker™ passes freely through cell-membranes, but once inside a cell, it is transformed into cell-impermeant reaction products and is retained in living cells through several generations. For the cytoplasmic staining, CellTracker™ Blue solution (20 μM final concentration) was added directly to the culture medium of an ~80% confluent 15-cm culture dish. Then the cells were transferred to LabTek™ chambered four-well coverglasses in an appropriate dilution and incubated for 3 hr at 37°C and 10% CO₂. For the plasma membrane and TNT staining, WGA Alexa Fluor® (1 mg/ml) was added directly to the culture medium (1/300) before microscopy.

High-resolution, brightfield fluorescence microscopy was performed with a Olympus IX70 microscope (Olympus Optical Co. Europa GmbH, Hamburg) equipped

with a 100× Plan Apo 100×/1.40 NA oilimmersion objective (Olympus Optical Co), a monochromator-based imaging system (T.I.L.L. Photonics GmbH, Martinsried, Germany), a tripleband filterset DAPI/FITC/TRITC F61-020 (AHF Analysetechnik AG, Tübingen, Germany) and a piezo z-stepper (Physik Instrumente GmbH & Co., Karlsruhe, Germany) (20). The imaging system was also equipped with a 37°C heating control device and a 5% CO₂ supply (Live Imaging Services, Olten, Switzerland). Dual channel image recordings were performed, the first channel at a wavelength of 555 nm recording the WGA Alexa Fluor®, the second channel at a wavelength of 400 nm recording the CellTracker™ Blue signal. For each channel, 40 planes were acquired, processed by using the deconvolution extension of TILLvision (T.I.L.L. Photonics GmbH), and resulting in stacks of grayscale unsigned integer 16 bits images with dimensions 520 × 688 × 40. Each pixel has an extension of 134 × 134 nm², summing up a total image area of 69.68 × 92.19 μm², and the separation between the focal planes was 300 nm.

Input Data and Processing Steps in the TNT Segmentation Procedure

To illustrate the data we are dealing with, a selection of four representative dual channel images belonging to separate 3D image stacks are shown in Figures 1a-1h. Notice the presence of noise, uneven illumination, and intracellular grains of similar intensity as cell borders in the left column of these images. Clearly visible TNTs are marked with arrows. These images represent the first and

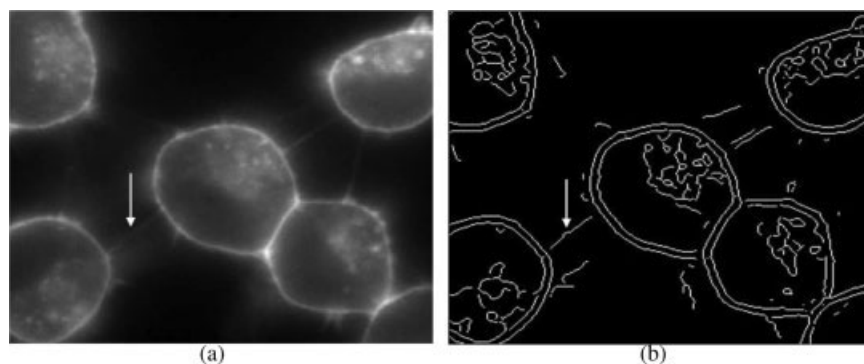


FIG. 4. Edge detection leads to the identification of cell borders and TNT candidates. Canny's edge detector was applied to the image in (a), resulting in a binary image (b) showing all edge components. The edge component that will be used for further demonstrations is labeled with an arrow.

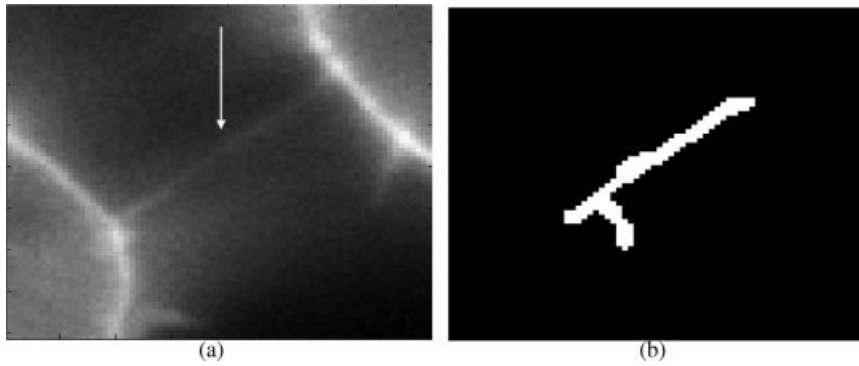


FIG. 5. Maximum projection of a TNT candidate from the edge image. The original image (a) shows a TNT. The corresponding maximum projection of its edge structure is seen in (b), which originates from the edge structure indicated by an arrow in Figure 4b. The maximum projection was later used for initializing a watershed segmentation.

second image channel from a given focal plane, magnified to better display details. The left column shows the first image channel, and the right column shows the corresponding second image channel displaying cells as bright regions. The second image channel was used to separate cells from background at high contrast. It allows to eliminate TNT candidates detected in cellular areas.

These depictions show the thin and elongated TNT structures that appear as straight lines connecting one cell to another. Typically, the width of the TNTs seen in fluorescence images is comparable with one third of the thickness of the imaged cell walls. The TNTs have notably darker gray levels than the cell walls, and their gray-level and noise characteristics vary little along their extension in 3D. They are surrounded by darker intercellular regions except at their endpoints where there is a seamless connection with the plasma membrane. However, the image recordings are hampered by moderate noise and blurring of fine details and in certain cases TNTs are located very close to each other, as in Figure 1g. Usually, the human eye is better than computers for shape detection, but even by a trained eye, it may be hard to decide whether a structure is a TNT or not. As a consequence, automated TNT detection is a challenging and error-prone image analysis task. Cultured PC12 cells are 3D objects forming a network of TNTs. Because of the distribution of plated cells, the TNTs are mainly propagating in the xy imaging plane. However, they are sometimes inclined, requiring a 3D tool for TNT detection. Our algorithm takes advantage of these properties of the TNTs, by applying projections from 3D to 2D. Provided that TNTs exist in tissue, which is left to be shown, their straight line appearance could change into bended struc-

tures because of the dense extracellular matrix. Further, one could expect TNTs to propagate equally in all spatial directions. Thus, for a tissue sample, a rotationally invariant approach would be necessary to detect TNTs.

For plated PC12 cells, we have chosen to approach the detection problem by searching the image for all significant edges occurring on background regions, since TNTs are intercellular structures. As a first *preprocessing step*, deblurring using RL deconvolution (21) was performed, assuming the focal plane images are Gaussian-like blurred. In all experiments, the RL algorithm was supplied with a Gaussian point spread function of size 5×5 pixels and standard deviation 5.

A general outline of the control flow of our algorithm, omitting the initial image restoration step (RL deconvolution), is given in Figure 2.

All algorithms and statistical evaluations in this paper were implemented in MATLAB 7.0.1 and executed on a 64bits 2.2GHz AMD processor running Linux. An average process takes ~ 20 min for a 3D stack. MATLAB was chosen for the implementation because of its broad library of built-in image processing functions. The code in our algorithm has been extensively vectorized to obtain computational speed, probably at the same order as compiled code. In the following, details from each processing step are described, and the results from each step as they apply to the data of Figures 1a and 1b are illustrated.

Description of Each Processing Step

Classification of cells and background. The cell marker channel was used for binary classification of each

FIG. 6. Minima seed regions for watershed segmentation. The sum image in (a) has a TNT candidate between the corresponding minima seed regions in (b). These seed regions were used for initializing a watershed segmentation to detect the ridge of the TNT candidate.

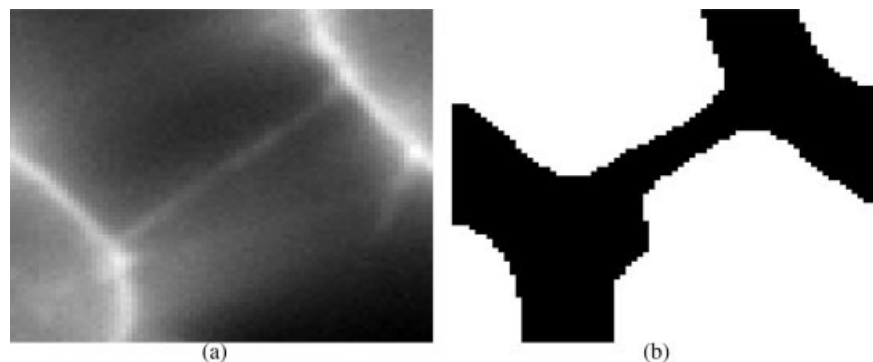




FIG. 7. The ridge of a TNT candidate and the cell borders have been found from watershed segmentation of Figure 6a using the initialization regions in Figure 6b.

pixel into cell or background. As seen in Figure 3a, the cell soma appears as high intensity regions in the cell marker channel. Applying a simple thresholding for segmentation of cells is unsuitable because of noise and uneven illumination. The boundaries of the cells are better characterized using an edge detector. Canny's edge detector was therefore used to mark the border between cells and background, and the closed regions were filled using morphological filling. By these means, a partition into "intracellular" and "extracellular" regions was obtained, displaying cells as white and background as black. The result of this processing step, applied to Figure 3a, is shown in Figure 3b.

Detection of TNTs. TNTs are structures occurring at a certain level above the substrate and they are usually not found in the uppermost planes of the 3D images from PC12 cells. Thus, the algorithm has been applied exclusively to the central 30 planes of the stacks, discarding the upper five and lower five planes in each stack to restrict computational time and reduce the number of false-positive TNT candidates. TNTs are structures with moderate grayscale values compared with cell borders. Consequently, screening for TNTs using intensity based segmentation methods will fail. However, they are thin and elongated with a relatively high gradient normal to their pointing direction, and therefore Canny's edge detector was ap-

plied to channel 1. This process, exemplified for Figure 4a, is shown in Figure 4b.

The smallest edge components were removed by thresholding since they were below the size limit for a reasonable evaluation. As a first step in the edge pruning, all edges inside the cells were removed, and the connected components outside the cells were labeled individually using first order neighborhood. To retain 3D information for each component into a 2D-image, the *maximum intensity projection* (MIP) was applied. In brief, assume that f is the 3D-image of the first channel. The MIP maps the image planes between f_m and f_n into a 2D-image which takes the maximum intensity values along the z direction. The maximum projection was calculated for each connected component in the edge image, the component ranging from plane m to n . The MIP was thus restricted to a limited number of planes. Figure 5b depicts the maximum projection of the component indicated by the arrow in Figure 4b. The image region corresponding to Figure 5b is shown in Figure 5a.

The cell regions (cf. Fig. 3b) and the eroded background regions were added into one single image. This created a binary image marking the inside and outside of the cells, omitting the cell borders. The projected structure of Figure 5b was subtracted from this binary image, and a morphological opening was performed to open up a pathway from one cell to another in the cases where it was possible. This created a final marker image, used as initialization to a watershed segmentation (22–24) for each connected component in the edge image. The watershed segmentation was employed to locate the crest lines of the high intensity edges. The minima marker image corresponding to the structure in Figure 5b is shown in Figure 6b where the minima initialization regions are labeled white.

Furthermore, only image regions close to the structure of interest were used in further calculations to save computational time and increase accuracy of the watershed algorithm. The watershed segmentation required boundaries of the minima marker regions that were sufficiently close to the edge structure of interest, if that was not the case, the watershed segmentation would often detect another crest of minor interest, still containing strong edge information.

TNTs are frequently crossing several planes. Therefore the *sum image* from plane m to n was used as input for

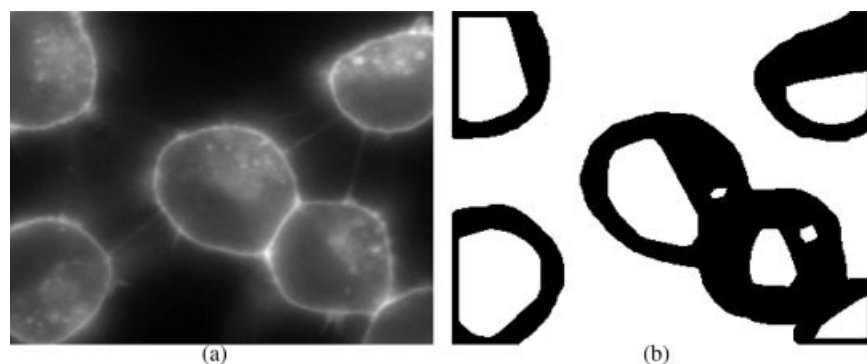


FIG. 8. Initialization regions for watershed segmentation of cells. The image (a) is assigned a minima marker image (b) that initializes the watershed segmentation of cells.

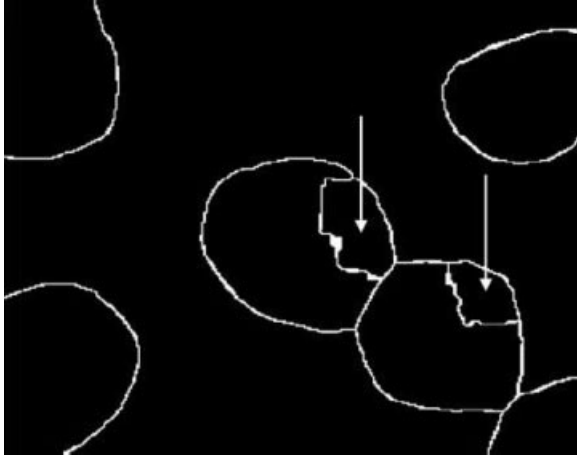


Fig. 9. Watershed segmentation of cells. The image shows the borders between the regions that appear from watershed segmentation of Figure 8a. Two regions marked with arrows are incorrectly assigned as individual regions because of oversegmentation.

watershed segmentation. Let f be the 3D-image of the first channel. For given $m \leq n$, let f_i , $i = m, \dots, n$ be plane i from the image stack. The sum projection $P_{\text{sum}}(f; m, n)$ is defined as

$$p_{\text{sum}}(f; m, n) = \sum_{m \leq i \leq n} f_i$$

This projection maps the image planes between f_m and f_n into a 2D-image which adds the intensity values along the z -direction. Consequently, the problems of TNTs frequently crossing several planes was minimized as the TNTs now were visible in their whole length inside the 2D projection. In addition, when adding multiple image planes close to each other, a stochastic noise suppression was obtained since the noise is assumed close to Gaussian and independent (when the effect of deconvolution is ignored). Summing *all* image planes in the 3D stack would blur the 2D projection too much, and at the same time blurring the TNTs. The projections from 3D onto 2D were therefore limited to the same *range as the current structure found by the edge detection*, thus enhancing the edge feature that was investigated. A normalization of (1) is possible, but not necessary, since a scaling factor will not influence the forthcoming watershed segmentation. A watershed segmentation was applied to the projected *sum image* in Figure 6a using the minima image in Figure 6b as initialization for the algorithm. The watersheds created, are depicted in Figure 7, labeling the ridge of the structure of interest.

The watershed segmentation was repeated for each and every edge structure in the edge image. It was not possible to perform the watershed segmentation for all connections simultaneously, since information would then get lost from the morphological opening in the case of close structures.

Watershed segmentation of each cell. In section “Classification of cells and background,” the image regions

covered by cells and background were acquired from the second image channel. However, this segmentation provides insufficient information about cell-to-cell borders of associated cells, only outlining the cell-to-background borders (cf. Fig. 3a). Therefore, to obtain an algorithm being able to determine between which pair of cells a TNT is crossing, a specific cell-by-cell segmentation was additionally required. To partition the first image channel (Fig. 8a) into meaningful regions that are separated by high intensity cell walls, a watershed transformation was used. The method is well described in literature (24–26), and the largest disagreements arise from the problem of creating suitable minima to initialize the watershed algorithm. Direct application of the watershed transform to a grayscale image f often leads to severe oversegmentation because of noise and image irregularities. To obtain the marker image, all minima in f not connected to the image border were filled. This was performed by filling the holes in f ([23, pp. 173, 174]) using morphological reconstruction by erosion (27) as implemented in MATLAB’s Image Processing Toolbox. One example of such binarized marker image is shown in Figure 8b, created for image f in 8(a).

The markers representing the background were verified using the complement of the cellular areas computed in section “Classification of cells and background,” representing high-accuracy markers for the background. When using minimum marker images, the watershed transformation resulted in a certain degree of oversegmentation. Each connected region from the watershed segmentation is named a watershed region. Figure 9 shows the borders between the watershed regions from Figure 8a. Notably, two small regions represent oversegmentation (Fig. 9, arrows).

Classification of watershed regions. To decide whether a particular TNT connected two cells, the watershed regions were classified as cells or background using the information of channel 2. Each region was placed on top of the binary cell image (cf. Fig. 3b) from step “Classification of cells and background,” and regions were classified as cells if they covered more cell- than

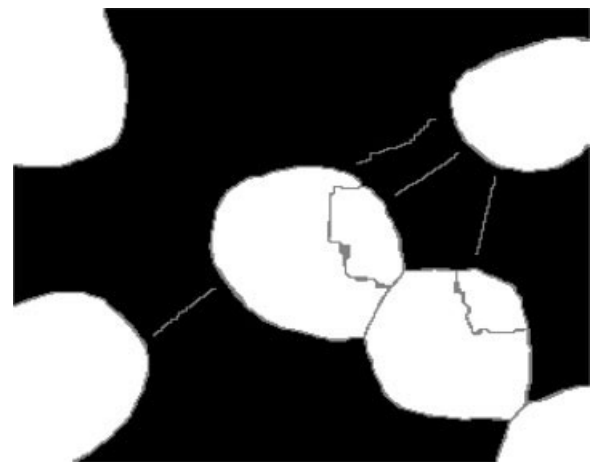


Fig. 10. Classification of cells, TNT candidates, and cell borders. White regions are cells, the gray lines are important edges, i.e., cell borders, TNTs, and artifacts, and the black regions are background.

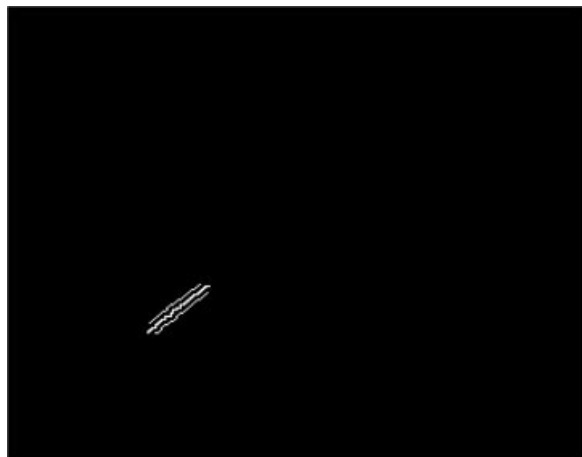


FIG. 11. Checking whether the TNT candidate is a high intensity edge or a flat region. A narrow, bilateral neighborhood following the TNT candidate defines a close neighborhood around the TNT candidate. The mean image intensity corresponding to the neighborhood pixels was compared with the mean image intensity on the TNT candidate itself.

background-pixels. Figure 10 depicts the classified regions of the watershed image in Figure 9.

Straight line criteria of TNTs, crossing between cells. TNTs are structures crossing on background from one cell to another, and it was checked whether this was true for each TNT candidate. The structure was dilated iteratively up to a predefined threshold, and the number of cells covered by the dilation was then counted, giving the number of cells close to the TNT candidate. Moreover, the Hough transformation for each TNT candidate was calculated. By comparing the minimum Hough transformation to a predefined threshold, it was decided whether the TNT candidate was approximately a straight line or not. If the connection was not a straight line, it was rejected as a TNT.

High intensity criteria of TNT candidates. A TNT is characterized by moderate grayscale values in a global sense, but locally their intensity values will be higher compared with their surroundings. A subtraction of the image intensities on two almost equal dilations of the TNT candidate, defined a narrow neighborhood on each side of the connection. This is illustrated in Figure 11 where the TNT candidate is surrounded by the two lines following it. The grayscale intensities on each TNT candidate were com-

pared with the intensities of its bilateral, narrow neighborhood. Insignificant differences implied removal of the TNT candidate as a false-positive TNT.

In some cases, artificial candidates passed through all preceding tests, candidates that are practically too small to be a TNT, covering only a few pixels. These were removed using a simple threshold value for the largest distance between the points in the candidate, they were anyway too short to undergo a correct TNT evaluation. The assumed real TNTs found at this stage, are shown in Figure 12b.

Method for Performance Evaluation

To test the robustness of our algorithm and avoid overfitting to specific image data, it has been tested on a separate data set not used for design and tuning of the numerical routines. A “true” identification of TNTs, obtained by manual labeling and counts have been performed by two different observers. One of them, (S.G.), an expert on TNT biology, was not involved in the algorithmic development or the computer vision experiments. The other person (E.H) has been responsible for the development of the automated method. In the cases of doubt, the manual counting rules were such that the TNT candidate in question was discarded. For a connection to be regarded as a true TNT, it must have been rated as TNT by both human observers. A false-positive TNT detection is the situation where an image feature is found to be a TNT by the program, but not rated as a TNT by the observers, or at most by one of the observers. A false-negative TNT detection occurs when both observers decide the structure to be a TNT, but the program misses. Note that this method for performance evaluation imposes a very strong criterion of success for the algorithm since it is calculated from the number of agreements of both the human raters. Thus, the success rate of the automated method will be a very conservative estimate.

RESULTS

The performance of the automated detection has been compared with manual TNT identification. Using the hold-out method for performance evaluation and the counting rules described in the section Method for Performance Evaluation, the automated detection was capable of locating 67% of the TNTs counted manually by the two observers. False-positive TNTs occurred more frequently than

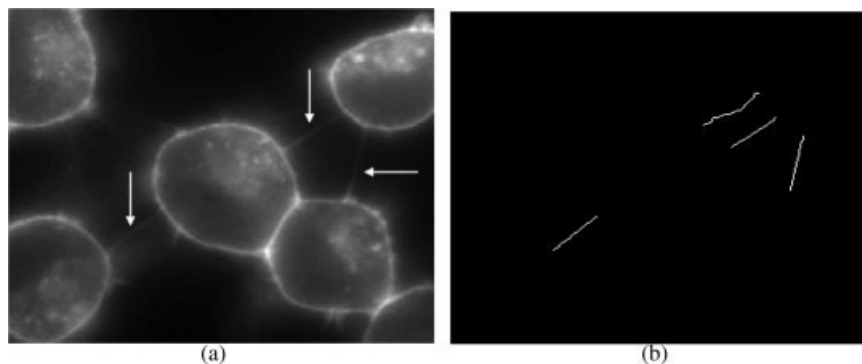


FIG. 12. Final detection of TNTs. All TNTs labeled by arrows in (a) have been automatically detected in (b).

Table 1
Numerical Results From Automated and Manual Detection of TNTs

Stack	Observer 1 count	Observer 2 count	1 and 2 agreements	Agreeing automated count	False negative	False positive	Success rate (%)
1	3	4	3	2	1	2	67
2	4	3	3	2	1	5	67
3	13	9	9	6	3	4	67
4	9	7	7	5	2	2	71
5	8	4	4	4	0	3	100
6	5	4	3	3	0	2	100
7	12	12	10	9	1	2	90
8	13	10	10	4	6	5	40
9	11	5	5	3	2	3	60
10	10	7	7	5	2	3	71
11	6	8	6	3	3	4	50
12	2	2	0	0	0	1	100
13	3	3	3	3	0	4	100
14	5	4	4	2	2	1	50
15	6	5	5	4	1	2	80
16	6	6	5	5	0	2	100
17	4	2	1	1	0	5	100
18	1	1	1	0	1	4	0
19	3	4	3	2	1	0	67
20	4	4	4	3	1	1	75
21	4	5	4	3	1	3	75
22	4	2	2	0	2	1	0
23	7	6	5	4	1	1	80
24	8	6	6	4	2	2	67
25	5	4	3	3	0	3	100
26	3	3	3	2	1	3	67
27	9	8	8	5	3	3	62
28	12	13	9	7	2	6	78
29	10	8	8	3	5	0	37
30	3	3	1	1	0	0	100
31	12	14	12	7	5	4	58
32	6	6	5	2	3	3	40
33	8	4	6	3	3	3	50
34	8	11	8	6	2	6	75
35	8	7	7	5	2	4	71
36	9	8	7	4	3	4	57
37	5	5	4	2	2	2	50
38	7	6	6	3	3	1	50
39	8	11	8	3	5	4	37
40	4	3	3	3	0	2	100
41	2	2	2	2	0	1	100
42	8	8	8	6	2	3	75
43	5	5	3	1	2	0	33
44	3	2	2	2	0	3	100
45	10	11	9	6	3	2	67
46	8	8	8	6	2	3	75
47	7	5	5	4	1	3	80
48	8	10	8	5	3	4	62
49	8	8	7	5	2	4	71
50	7	7	6	5	1	4	83
51	9	9	9	5	4	3	56
Total	343	312	275	183	92	140	67

false negative. However, false-positive TNTs are not necessarily really false TNTs, since the automated method in many cases found structures that resemble TNTs, but one or both human observers had missed them in their counting. Table 1 shows the number of TNTs in each 3D image stack used for performance evaluation. The columns show the TNTs counted by both observers, the agreements between them, the number of automatically correctly classified TNTs, the false negative and positive, and the success rate (%).

The last row in Table 1 displays the overall results; the total number of TNTs counted by each of the two observers and their agreements, the number of automatically correctly classified TNTs, the percentage false negative, the percentage false positive, and the final mean success rate. The final mean success rate has been calculated as the rate between "Agreeing automated counts" and "1 and 2 agreements." The "ground truth," taken as agreement between two human observers, needs some justification. In such challenging and demanding image processing prob-

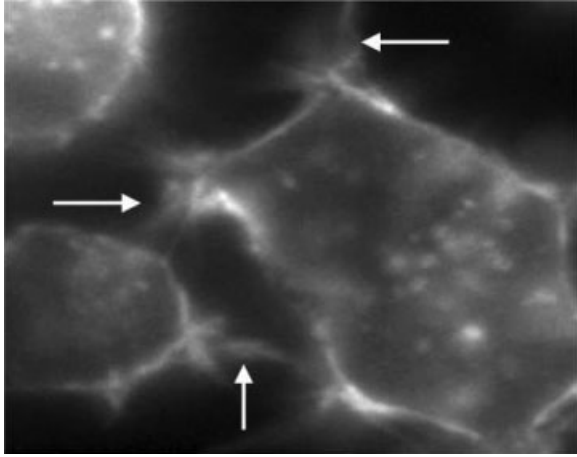


FIG. 13. Sharp edged filopodia-like cell structures shown by arrows. Most false-negative and false-positive automated TNT detections are because of high intensity image structures resembling TNTs. The case of cells close to each other is particularly challenging.

lems as TNT detection, a true solution is hard to achieve. Still, a trained human eye is probably the best tool available to establish a gold standard. For the current TNT detection experiment, a one-way ANOVA analysis reveals no significant difference ($P = 0.24$) of mean TNT counts ($\mu_1 = 6.7$, $\mu_2 = 6.1$, $\mu_a = 6.3$) across all 51 stacks obtained by observer 1, observer 2, and the automated method, respectively. The count for the automated method was obtained by adding “Agreeing automated count” and “False positive.” On the other hand, the two human observers turned out to correlate more to each other than to the automated method. Pearson correlation coefficient applied to the observations of the two human observers and the automated method showed a significant correlation ($\alpha = 0.05$) between the two human observers ($P < 0.0001$), in contrast to nonsignificant correlations between the automated method and each of the observers ($P = 0.42$ and $P = 0.17$). This finding justifies using the decisions by human observers as “ground truth,” since our independent observers have a high level of agreement.

From our TNT evaluation experiments, TNT detection is more likely to fail in the cases where the cells have close proximity or show large irregularities. An example of such typical irregularities is demonstrated in Figure 13, where high intensity structures and sharp edges of filopodia-like structures (Fig. 13, arrows) are crossing between cells, misleading the automated detection.

The presence of these edges satisfies the TNT criteria used for the automated detection. The digital data sets also allow further statistical measures of properties of TNTs like length histogram, number of TNTs connections per cell, and their slope inside the stack. To illustrate the power of the automated evaluation, we have performed measurements of length for each TNT. A 3D reconstruction of the TNTs was possible for length calculations since the algorithm keeps record of the projection range for each TNT candidate at all steps of the processing chain. The length statistics was obtained using the maximum Eu-

clidean distance between all pixels in the TNT, adjusted for the voxel anisotropy. Integration in space was redundant since TNTs always appear as straight lines. The distribution of TNT length in our sample is illustrated in Figure 14, statistics which is not feasible to obtain by manual methods. The length distribution of TNTs indicates that there is a high frequency of short TNTs between $1 \mu\text{m}$ and $4 \mu\text{m}$. This may suggest that there is an optimal distance between cells for TNT formation.

DISCUSSION

TNTs are newly discovered structures connecting mammalian cells. It emerges that these structures play an important role in cell-to-cell communication. Using human resources for counting them is demanding, time consuming, and subject to interobserver variability. By orchestrating various well-known image processing techniques, we have developed a new and versatile method for detection of TNTs in fluorescence microscope images of cultivated cells. Using our sequence of algorithms for finding TNTs and connecting cells in two channel fluorescence images of cultured PC12 cells from rat, we obtained a success rate of 67% applying a hold-out evaluation method and using manual labeling as “gold standard.” Moreover, the occurrence of false-positive TNTs was more frequent than false negatives.

The success rate of the TNT detection depends critically on proper classification of cells and background. This part has been accomplished by using a biological cell marker image in combination with mathematical image processing techniques. Furthermore, a proper detection of TNTs also depends on cell cultures with optimal and reproducible growth conditions. Under normal cell culture conditions, cells often grow in close proximity which makes it difficult to detect TNTs. This problem is illustrated in Figure 13. To circumvent this problem, cells should be grown on specific matrix patterns (28) which guarantee more standardized cell culture conditions. In particular, this would ensure a certain distance between

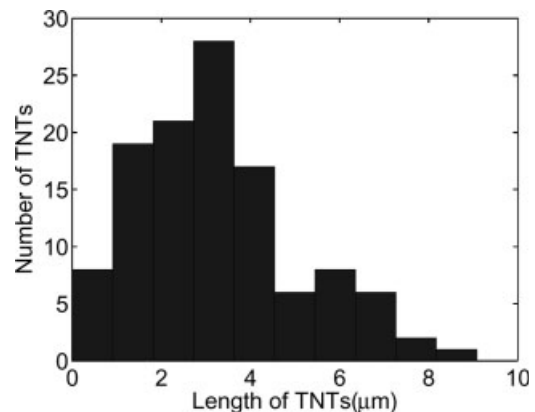


FIG. 14. Distribution of the 3D length of TNTs which have been detected automatically. Small TNTs between $1 \mu\text{m}$ and $4 \mu\text{m}$ connecting close cells are dominating.

cells, thus improving the algorithmic ability to locate TNTs.

The automated detection also allowed estimation of statistical information on selected properties of TNTs in addition to counts. One important parameter would be to know how many TNT connections a cell is generating. This parameter might vary according to different biological conditions as they occur during pathological processes. Provided that TNTs are involved in certain pathological states of multicellular organisms, it can be of great value to either block or enhance their function. In this respect, the screening of drugs for modulating TNT formation and function would benefit from automated programs suitable for quantitative analysis of TNTs. In this way, the effect of drugs could be evaluated by high throughput screening.

ACKNOWLEDGMENTS

The authors thank Aurora Martinez for computational resources and Roland Kaufmann for proof reading. The authors are also grateful to the Molecular Imaging Center (MIC) at the Department of Biomedicine, University of Bergen. The authors thank H. Bading for lab space and infrastructure at the Department of Neurobiology, University of Heidelberg. The authors are grateful for the constructive comments from the anonymous reviewer.

LITERATURE CITED

- Rustom A, Saffrich R, Markovich I, Walther P, Gerdes HH. Nanotubular highways for intracellular organelle transport. *Science* 2004;303:1007-1010.
- Gerdes HH, Rustom A. Tunneling nanotubes: Cell-cell channels in animal cells. In: Baluska F, Volkmann D, Barlow PW, editors. *Cell-Cell Channels*. Georgetown: Landes Bioscience; 2005.
- Onfelt B, Nedvetzki S, Yanagi K, Davis DM. Cutting edge: Membrane nanotubes connect immune cells. *J Immunol* 2004;173:1511-1513.
- Watkins SC, Salter RD. Functional connectivity between immune cells mediated by tunneling nanotubules. *Immunity* 2005;23:309-318.
- Cilia ML, Jackson D. Plasmodesmata form and function. *Curr Opin Cell Biol* 2004;16:500-506.
- Wu K, Gauthier D, Levine MD. Live cell image segmentation. *IEEE Trans Biomed Eng* 1995;42:1-12.
- Nattkemper TW, Twellmann T, Ritter H, Schubert W. Human vs machine: Evaluation of fluorescence micrographs. *Comput Biol Med* 2003;33:31-43.
- Bengtsson E, Wählby C, Lindblad J. Robust cell image segmentation methods. *Pattern Recognit Image Anal* 2004;14:157-167.
- Carpenter AE, Thouis RJ. The CellProfiler, Cell Image Analysis Software Project. Whitehead Institute for Biomedical Research and MIT C SAIL. <http://jura.wi.mit.edu/cellprofiler>.
- Wählby C, Lindblad J, Lindblad J, Vondrus M, Bengtsson E, Björkstén L. Algorithms for cytoplasm segmentation of fluorescence labelled cells. *Anal Cell Pathol* 2002;24:101-111.
- Yang F, Jiang T. Cell image segmentation with kernel-based dynamic clustering and an ellipsoidal cell model. *J Biomed Inform* 2001;34:67-73.
- Garrido A, Perez de la Blanca N. Applying deformable templates for cell image segmentation. *Pattern Recognit* 2000;33: 821-832.
- Mouroutis T, Roberts S, Bharath A. Robust cell nuclei segmentation using statistical modelling. *Bioimaging* 1998;6:79-91.
- Nath Di, Depona T, Acharya C. Report from Department of Computational Biosciences, Arizona State University, Tempe, AZ. DNA protein interactions: Studying the 'bendability' of DNA to accommodate proteins using MATLAB. 2004. http://math.la.asu.edu/~cbs/pdfs/projects/Fall_2004/Group4_report.pdf
- Niesmistö A, Dunmire V, TliHarja O, Zhang Wai, Shmulevich I. Robust quantification of in vitro angiogenesis through image analysis. *IEEE Trans Med Imaging* 2005;24:549-553.
- Lomenie N, Barbau J, Triassanz R. Integrating textural and geometric information for an automatic bridge detection system. Proceedings of the 2003 International Geosciences And Remote Sensing Symposium, IGARSS 2003, Toulouse, France.
- Jeong JH, Takagi M. Extraction of bridge positions from IKONOS images for accuracy control of bridge database. Proceedings of the 23rd Asian Conference on Remote Sensing, Kathmandu; 2002; (172). ACRS/Asian Association on Remote Sensing, Tokyo, Japan.
- Block T, Kin C, Breckenridge BM. Mutants of PC12 cells with altered cyclic AMP responses. *Mol Cell Biol* 1984;4:2091-2097.
- Greene LA, Tischler AS. Establishment of a noradrenergic clonal line of rat adrenal pheochromocytoma cells which respond to nerve growth factor. *Proc Natl Acad Sci U S A* 1976;73:2424-2428.
- Rustom A, Gerlich D, Rudolf R, Heinemann C, Eils R, Gerdes HH. Analysis of fast dynamic processes in living cells: High-resolution and high-speed dual-color imaging combined with automated image analysis. *BioTechniques* 2000;28:722-730.
- Carasso AS. Linear and nonlinear image deblurring: A documented study. *SIAM J Numer Anal* 1999;36:1659-1689.
- Gonzalez RC, Woods RE. *Digital Image Processing*. Boston, MA: Addison-Wesley; 1992.
- Soille P. *Morphological Image Analysis: Principles and Applications*. Berlin: Springer-Verlag; 1999.
- Vincent L, Soille P. Watersheds in digital spaces: An efficient algorithm based on immersion simulations. *IEEE Trans Pattern Anal Mach Intell* 1991;13:583-598.
- Lin Umesh GA, Olson K, Guzowski JF, Barnes CA, Roysam B. A hybrid 3D watershed algorithm incorporating gradient cues and object models for automatic segmentation of nuclei in confocal image stacks. *Cytometry A* 2003;56:23-26.
- Adiga PSU. Integrated approach for segmentation of 3D confocal images of a tissue specimen. *Microsc Res Tech* 2003;54:260-270.
- Vincent L. Morphological grayscale reconstruction in image analysis: Applications and efficient algorithms. *IEEE Transac Image Process* 1993; 2:176-201.
- Arnold M, Cavalcanti-Adam EA, Glass R, Blummel J, Eck W, Kantlehner M, Kessler H, Spetz JP. Activation of integrin function by nanopatterned adhesive interfaces. *Chemphyschem* 2004;5:383-388.